

## Journal Pre-proof

Identifying recurrent and persistent landslides using satellite imagery and deep learning: A 30-year analysis of the Himalaya

Tzu-Hsin Karen Chen, Mark E. Kinsey, Nick J. Rosser, Karen C. Seto



PII: S0048-9697(24)01300-7

DOI: <https://doi.org/10.1016/j.scitotenv.2024.171161>

Reference: STOTEN 171161

To appear in: *Science of the Total Environment*

Received date: 29 October 2023

Revised date: 20 January 2024

Accepted date: 19 February 2024

Please cite this article as: T.-H.K. Chen, M.E. Kinsey, N.J. Rosser, et al., Identifying recurrent and persistent landslides using satellite imagery and deep learning: A 30-year analysis of the Himalaya, *Science of the Total Environment* (2023), <https://doi.org/10.1016/j.scitotenv.2024.171161>

This is a PDF file of an article that has undergone enhancements after acceptance, such as the addition of a cover page and metadata, and formatting for readability, but it is not yet the definitive version of record. This version will undergo additional copyediting, typesetting and review before it is published in its final form, but we are providing this version to give early visibility of the article. Please note that, during the production process, errors may be discovered which could affect the content, and all legal disclaimers that apply to the journal pertain.

© 2024 Published by Elsevier B.V.

# Identifying recurrent and persistent landslides using satellite imagery and deep learning: a 30-year analysis of the Himalaya

Tzu-Hsin Karen Chen<sup>a,b,c\*</sup>, Mark E. Kincey<sup>d</sup>, Nick J. Rosser<sup>e</sup>, and Karen C. Seto<sup>c</sup>

<sup>a</sup>Department of Urban Design and Planning, University of Washington, Seattle, WA, USA

<sup>b</sup>Department of Environmental and Occupational Health Sciences, University of Washington, Seattle, WA, USA

<sup>c</sup>Yale School of the Environment, Yale University, New Haven, CT, USA<sup>d</sup>School of Geography, Politics and Sociology, Newcastle University, Newcastle upon Tyne, UK

<sup>e</sup>Department of Geography, Institute of Hazard, Risk, and Resilience, Durham University, Durham, UK

\*corresponding author: Tzu-Hsin Karen Chen

Email: kthchen@uw.edu

Address: 3980 15th Avenue NE Seattle, WA 98195

## Abstract

This paper presents a remote sensing-based method to efficiently generate multi-temporal landslide inventories and identify recurrent and persistent landslides. We used free data from Landsat, nighttime lights, digital elevation models, and a convolutional neural network model to develop the first multi-decadal inventory of landslides across the Himalaya, spanning from 1992 to 2021. The model successfully delineated more than 265,000 landslides, accurately identifying 83% of manually mapped landslide areas and 94% of reported landslide events in the region.

Surprisingly, only 14% of landslide areas each year were first occurrences, 55-83% of landslide areas were persistent and 3-24% had reactivated. On average, a landslide-affected pixel persisted for 4.7 years before recovery, a duration shorter than findings from small-scale studies following a major earthquake event. Among the recovered areas, 50% of them experienced recurrent landslides after an average of five years. In fact, 22% of landslide areas in the Himalaya experienced at least three episodes of landslides within 30 years. Disparities in landslide persistence across the Himalaya were pronounced, with an average recovery time of 6 years for Western India and Nepal, compared to 3 years for Bhutan and Eastern India. Slope and elevation emerged as significant controls of persistent and recurrent landslides. Road construction, afforestation policies, and seismic and monsoon activities were related to changes in landslide patterns in the Himalaya.

**Keywords:** landslide inventory, landslide evolution, vegetation recovery, multi-temporal, spatiotemporal analysis, machine learning

## 1. Introduction

Landslides triggered by earthquakes and extreme rainfall are known to persist and/or reoccur over time, posing ongoing challenges to infrastructure and human safety (Hovius et al., 2011; Lin and Lin, 2015; Marc et al., 2015; Kincey et al., 2021). Their impacts can affect communities and landscapes for years, sometimes decades (Mansour et al., 2011; Chen et al., 2021). Such effects are apparent at both large-scale over extensive areas, such as that impacted by an earthquake (e.g., Chen et al., 2019; Kincey et al., 2023), or at individual landslides or catchments (e.g., Samia et al., 2017; Temme et al., 2020). At both scales, data describing the spatial and temporal nature of landslides, would allow us to characterise their persistence (*how long do landslides remain in the landscape after they have occurred?*) and recurrence (*how often landslide occur in the same location more than once*). This knowledge is crucial for unpicking the components of long-term landslide hazard and risk, as well as understanding the physical and anthropogenic factors influencing landslide evolution (Gariano and Guzzetti, 2016; Jones et al., 2021; Muñoz-Torrero Manchado et al., 2021). Comparative analyses of these data across different territories can aid in resource allocation, mitigation and recovery strategies (Lee and Jones, 2023). However, the scarcity of comprehensive, multi-temporal landslide datasets, which are time-intensive and costly to produce, currently limits our understanding of persistent and recurrent landslides.

Optical remote sensing offers a proven approach for the multi-temporal analysis of landslides. Numerous studies have utilized expert knowledge to visually interpret landslides from time-series satellite data, enabling the identification of shifting landslide patterns (Fan et al., 2018; Jones et al., 2021; Kincey et al., 2021). However, such large-scale manual mapping is both time-

consuming and open to potential inaccuracies due to the subjectivity involved in the digitization of individual landslides (Meena and Tavakkoli Piralilou, 2019). In contrast, while automated analysis of satellite imagery alone may not provide sufficiently detailed information on all relevant factors pertinent to landsliding such as ground water, it can offer valuable information on vegetation cover and density, a crucial indicator of previous landslides and surface recovery (Shen et al., 2020). As optical satellite images can describe the distribution, they hold the potential to measure persistence and recurrence of landslides across large areas and over long time periods.

Automated methods of mapping landslides, such as thresholding vegetation indices from satellite time series to identify likely landslide footprints, have been developed to create multi-temporal landslide inventories and evaluate surface recovery (Behling et al., 2014; Behling et al., 2016; Yunus et al., 2020; Chen et al., 2021). By examining changes in vegetation index, studies can estimate the timing of landslide initiation and recurrence (Muñoz-Torrero Manchado et al., 2021). It is however important to note that the threshold for identifying landslides from a vegetation index can vary across landscapes, especially across elevation or precipitation gradients. This variability poses a challenge when attempting to apply a universal threshold at scale across extensive transboundary regions, such as the Himalaya. As a result, most existing multi-temporal analyses of landslides focus on catchment areas or earthquake affected regions to track landslide changes following a major disturbance. At larger scales, the occurrence, persistence and recurrence of landslides can be influenced by various factors such as climate change, infrastructure development, and the interplay between landslide preconditioning and triggering factors, which each exhibit spatial variations and require large-scale information to assess the resultant landslide dynamics.

In this study, we develop a methodology to identify the dynamic properties of landslide recurrence and persistence over a large geographic region. This large-scale analysis is an advance over existing remote sensing of landslide studies which identify a single landslide event or for a relatively small geographic region. Machine learning models can set up complex thresholds of surface reflectance for landslide detection using data-driven approaches, and so are able to map landslides across large extents (Chen et al., 2019). We use such an approach to generate a 30-year inventory of landslide scars using publicly available satellite data and deep learning techniques. Then, we validate the method using multiple landslide catalogs from media reports and manually mapped high-resolution data. The approach unveils the distribution and timing characteristics including first occurrence, persistence, and recurrence of landslides over 30 years across the Himalaya.

## 2. Study area

Our study area is the contiguous Himalaya mountain arc including the Indian states of Jammu and Kashmir, Himachal Pradesh, Uttarakhand (hereafter Western India), Sikkim, and Arunachal Pradesh (hereafter Eastern India), and the countries of Nepal and Bhutan (Fig. 1). As one of the most geologically active mountain regions, the Himalaya is experiencing rapid change, including expansion of built-up areas, infrastructure development and social and political change (Tiwari et al., 2018; Chen et al., 2023). We focused on areas below 4000 m elevation and aim to identify landslides that could pose risks to the population. Areas above this elevation are sparsely populated, and identifying landslides becomes challenging due to spectral similarities with the surrounding landscape above the tree line. The study area spans a land area of 365,021 km<sup>2</sup>.

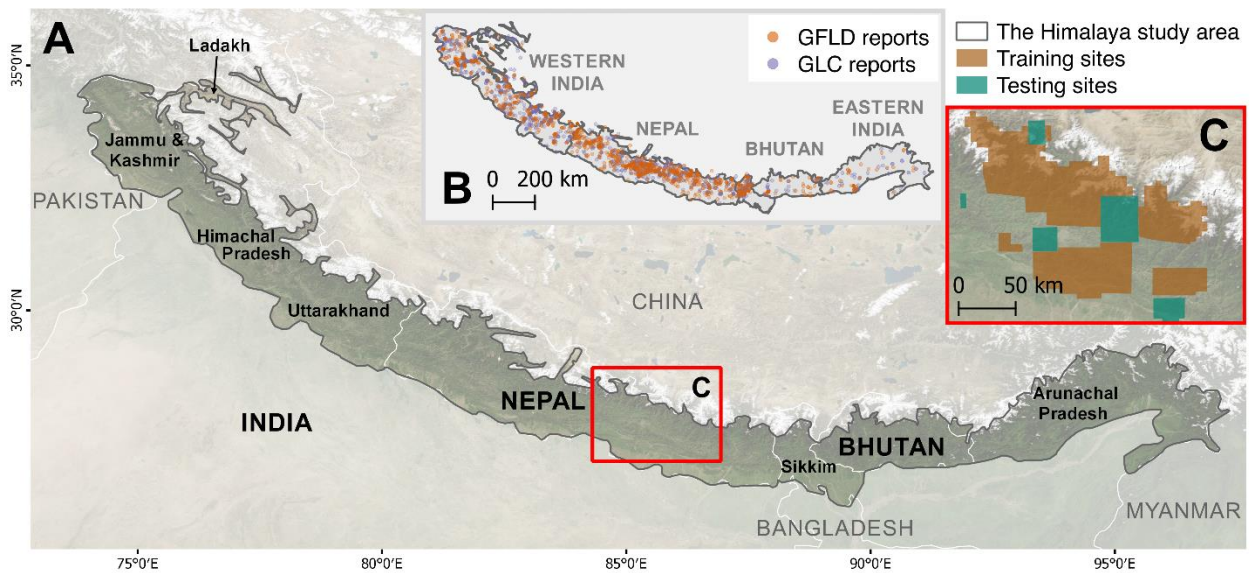


Fig. 1. (A) The Himalaya study area outlined in black where we mapped landslides through time, overlaid with topography from NASA's Blue Marble seamless image mosaic, (B) landslide reports across the Himalaya, represented by dots sourced from the Global Landslide Catalog (GLC) and the Global Fatal Landslide Database (GFLD), serve as the first testing dataset (Kirschbaum et al., 2010; Froude and Petley, 2018), and (C) manually mapped landslide data in Central and Western Nepal, which serve as training dataset and the second testing dataset for our machine learning model.

### 3. Data and methodology

#### 3.1 Satellite data

To ensure the replicability of our methodology for identifying landslides through time, we leveraged free satellite data with global coverage (Fig. 2). We selected relevant datasets known for their predictive capabilities in landslide analysis, including optical satellite images, nighttime light images, and topography data, and obtained them from Google Earth Engine (Reichenbach et al., 2018; Chen et al., 2019; Tehrani et al., 2022). Optical satellite images capture the spectral contrast of bare ground exposed by landslides from surrounding vegetation, where the landslide clears the surface material from the slope. Nightlight data aid in distinguishing landslides from visually similar features associated with human settlements and quarries. Additionally, slope is a key contributor to conditions that favor landsliding, such as the movement of water and the increase of shear stresses. As vegetation density typically varies along an elevation gradient, incorporating elevation into the deep learning model can be beneficial as it allows for the automatic exploration of interactive weights between elevation and surface reflectance. Hydrological networks denote the cells with rivers and can potentially help separate landslides from spectrally similar river gravels (Reichenbach et al., 2018). Mapped landslide inventories derived from sub-seasonal imagery are known to be sensitive to fluctuations in vegetation encroachment into landslide scars (Kincey et al., 2023). These largely predictable and small magnitude variations in sum can mask longer-term incremental changes in landslide characteristics, and hence we deliberately compared the same period between years, rather than within year changes.

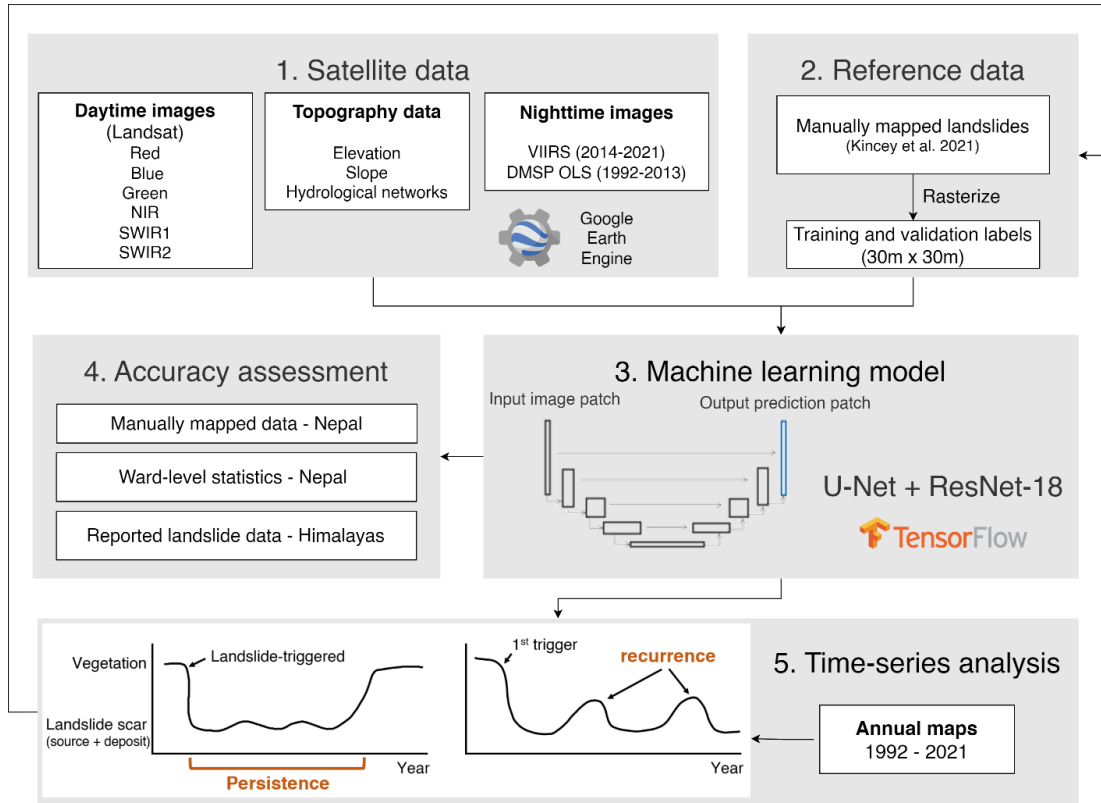


Fig. 2. Flowchart of the identification of landslides and their recurrence and persistence based on open-access Landsat daytime imagery, the digital elevation model, and the Defense Meteorological Satellite Program (DMSP) and the Visible Infrared Imaging Radiometer Suite (VIIRS) nighttime imagery datasets.

### 3.1.1 Daytime images

We obtained all available Landsat surface reflectance data from atmospherically corrected Collection 2, Tier 1, as well as the Quality Assessment band that we used to remove pixels covered by clouds, cloud shadows with a high confidence level, and scan-line corrector (SLC)-off gaps (USGS, 2020). This includes the blue, green, red, near-infrared, first and second shortwave infrared bands at 30-m spatial resolution. We collected all available images from

February to July to avoid low-quality observations affected by snow and cloud cover, while remaining close to the pre-monsoon period (i.e., January to May) covered by the training data from Kinsey et al. (2021). Additionally, we used a three-year window, including the target year, the previous year, and the following year to increase the number of high-quality observations. We then calculated the 40<sup>th</sup> percentile among available observations per pixel to represent the pre-monsoon reflectance of the middle year. This resulted in a total of 30 pre-monsoon image composites, covering the period from 1992 to 2021, at 30-m resolution for the Himalaya. The resolution defines the minimum size threshold of the landslides that we are able to detect, which is the size of a single pixel, 900 m<sup>2</sup>. We standardized all images using the 98<sup>th</sup> percentile of surface reflectance over the study area and years.

### 3.1.2 Nighttime images

We collected nighttime light imagery from the Defense Meteorological Satellite Program (DMSP) and the Visible Infrared Imaging Radiometer Suite (VIIRS). The VIIRS data are preferable as it has a finer resolution (463 m) than the DMSP data (1,000 m). Because VIIRS data are not available before 2014, we incorporated nighttime light imagery from the DMSP spanning 1992-2013 and the VIIRS for 2014-2021. We utilized processed DMSP data from the Consistent And Corrected Nighttime Light Dataset (Zhao et al., 2022). The VIIRS data were monthly average radiance composites and we transformed them into annual median values. Both datasets were resampled to 30-m resolution to match the daytime images. To account for the different luminosity units between VIIRS and DMSP, we used the method proposed by Chen et al. (2019) to generate VIIRS-like DMSP data with linear regression ( $R^2 = 0.59$ ).

$$V' = 0.157486 + 0.1249074 \times D$$

where  $V'$  denotes the VIIRS-like DMSP data and  $D$  denotes the original DMSP data.

### *3.1.3 Topography data*

Our topographical variables include elevation, slope, and hydrological networks. We used NASA's digital elevation model (DEM), which is the 2000 reprocessing of the Shuttle Radar Topography Mission data (Jpl, 2020). These data were remotely sensed by radar interferometry with a resolution of 1 arc-second and improved by using ICESat GLAS data for control. Slope is derived by determining the highest magnitude first derivative across each cell of the elevation in Google Earth Engine. We used HydroSHEDS to represent hydrological networks, which is also based on NASA's digital elevation model (Lehner et al., 2008).

## **3.2 Reference data**

### *3.2.1 Visually interpreted landslide data*

We used manually mapped landslide data based on an area of 25,575 km<sup>2</sup> from Central and Western Nepal reported in Kinney et al. (2021) as training and testing data for the machine learning model. This dataset has the advantage of: (1) being internally consistent; (2) having a systematically collected time-series of data; (3) being mapped from imagery of a resolution (i.e. Sentinel-2) better than our input satellite imagery (4) being mapped from an area that encompasses elevation, slope, land use and land cover; and climate typical of much of the wider Himalaya. The boundary of individual landslides, including combined source areas and deposits, was identified by the spectral contrast between exposed sediment or bedrock within the landslide and the surrounding vegetation. We used the data of 2016-2019 because the landslides in this period are generated from higher resolution Sentinel-2 images (10 m) and are of better quality

than our input satellite data. From 2016 to 2019, the number of landslides recorded in each pre-monsoon period ranged from 15,627 to 17,641. We converted the vector dataset into a  $30\text{ m} \times 30\text{ m}$  raster dataset to be consistent with the input satellite data.

We divided Kincey et al.'s dataset into training and testing data, with similar coverage of high-, mid-, and low-elevation areas (Fig. 1). Then, for the training data, we further split it into 80% and 20% for training and validation for the deep learning model's parameterization. We also aggregated the testing data by wards, which are the local government entities in Nepal, and Kincey et al.'s dataset includes 131 wards.

### *3.2.2 Reported landslide data*

To assess the model's applicability across the Himalaya, we utilized two landslide impact and occurrence catalogs: the Global Landslide Catalog (GLC) and the Global Fatal Landslide Database (GFLD) (Kirschbaum et al., 2010; Froude and Petley, 2018). Both catalogs focus on precipitation-triggered landslides only, with the GFLD specifically highlighting events causing human casualties, and both being heavily reliant upon event reporting which results in an inherent bias to inhabited areas. The GFLD recorded 1,000 landslide events in the Himalaya from 2004 to 2017, while the GLC documented a total of 1,268 events from 2007 to 2017. Latitude and longitude information in the catalogs were estimated from location names found in newspapers, government or scientific reports, providing an average precision of 5 km for the GFLD.

### ***3.3 Machine learning model***

The convolutional neural network (CNN) works by identifying patterns in the stack of satellite data that correspond to landslide and non-landslide examples from training data. The first step involves preparing pairs of satellite images and training labels in a "patch" format, which serves as the fundamental data unit for a CNN. CNNs showed higher accuracies than other machine learning models that do not automatically utilize spatial information for landslide detection (Ghorbanzadeh et al., 2019). A patch is a small image extracted from a portion of the training data that provides spatial information, with dimensions of  $n \times n$  pixels. Once the model begins its training process, we feed the model with various sets of parameters, such as learning rate, patch size, and loss function, to optimize its performance. The validation data is then utilized to determine the most favorable parameter sets. The model returned an output image of landslide probability, ranging from 0-1. In order to convert the probability into a binary landslide map, we conducted an iterative resampling process and measured accuracies across a range of probability thresholds. Through this analysis, we determined that a threshold of 0.14 achieved the desired precision-recall trade-off (Fig. 3). Finally, we assess the accuracy of the final model using independent testing data that was neither used during training nor validation.

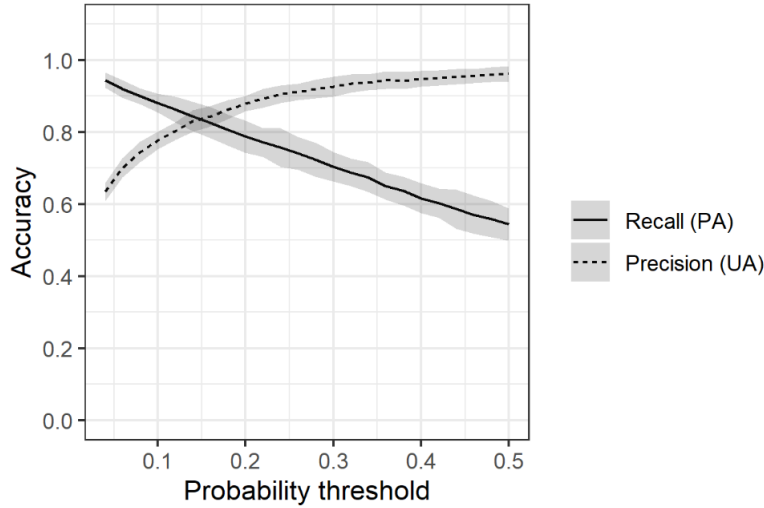


Fig. 3. Sensitivity analysis of the accuracy trade-offs with respect to the probability threshold used to classify the occurrence of landslides. Gray shading indicates the 95% confidence interval.

### 3.3.1 The U-Net architecture

We utilized the U-Net architecture as our CNN segmentation model to estimate the probability of a pixel being a landslide scar (Ronneberger et al., 2015). The U-Net has demonstrated its efficacy in land cover mapping in mountainous regions, where spectral similarities among different land covers exist (Chen et al., 2023). Unlike scene-based CNN, which assign a single label for each image patch, the U-Net architecture enables the extraction of spatial information pertaining to landslides across various scales while preserving spatial resolution between the input and output images. For the encoder, we employed the ResNet-18 backbone (He et al., 2016). Our implementation of the model utilized the Python packages TensorFlow and segmentation\_models.

### 3.3.2 Parameterization

The U-Net models were trained with the Adam optimizer (Kingma and Ba, 2014). Based on experimentation, we used an initial learning rate of 0.001, a decay rate of 0.8, a batch size of eight, and 40 epochs for training. We stratified and split original training data into training (80%) and validation sets (20%) to validate the stopping point during training. To address class imbalance, we combined Dice loss and Focal loss as the loss function. Dice loss minimizes overall errors, while Focal loss assigns higher weights to challenging examples (i.e., landslides). The ratio between Dice loss and Focal loss was set to 1:100 based on initial experiments. We used a patch size of  $64 \times 64$  pixels, as it provided higher accuracy than  $32 \times 32$  pixels for our U-Net model.

### 3.4 Accuracy assessment

Our accuracy assessment comprised three components. First, we evaluated the model's performance in predicting visually interpreted landslides from higher resolution images (i.e., Sentinel-2) and examined the impact of different input features on its accuracy. In the testing areas, we randomly sampled 400 landslide and 2,800 non-landslide points, with an accuracy standard error of 1%. We tested accuracies for different input combinations: daytime images alone, addition of topographical features and nighttime images, and varying training data duration (one, two, and three years).

Each data point was evaluated as one of four validation categories: true positive (TP), true negative (TN), false negative (FN), false positive (FP). Based on these categories, we calculated overall accuracy ( $(TP + TN) / (TP + TN + FP + FN)$ ), precision ( $TP / (TP + FP)$ ), recall ( $TP / (TP$

+ FN)), and F1 score  $((2 \times \text{precision} \times \text{recall}) / (\text{precision} + \text{recall}))$ . The precision represents the model performance in reducing landslide overestimation, recall refers to the ability to minimize landslide underestimation, and F1 score is the harmonic mean of recall and precision.

In the second component, we evaluated the model's performance in detecting historical landslide events across the broader Himalayan region. We organized the GFLD and GLC datasets by year and season, specifically the pre-monsoon (January-May,  $N = 419$ ) and post-monsoon (June-November,  $N = 1,849$ ) seasons. During testing, we utilized the pre-monsoon reports from a given year and the post-monsoon reports from the previous year since the model was trained using observed landslide scars from the pre-monsoon period. We calculated the detection rate (recall) of our model for each year. Considering the limitations of spatial precision in crowdsourced landslide databases, as documented by Froude and Petley (2018), we adopted a 5-km buffer to test whether the model can detect events in the surrounding area of the GFLD and GLC coordinates.

Third, we investigated potential biases in administrative interpretation at the ward level. For each ward, we calculated the landslide area, landslide areal density, and the number of landslide objects using the machine learning model's output. We then correlated these metrics with the reference metrics derived from visually interpreted data and analyzed the geographic context of wards experiencing under- or over-estimation. We used  $R^2$  and scatter plot to present correlation and bias.

### 3.5 Time-series analysis

After testing the model, we applied it to generate an annual landslide inventory from 1992 to 2021. We derived the attributes related to persistence and recurrence at both the annual and aggregated levels in R (see the code in the data availability statement). At the annual level, the total landslide area each year consisted of those that were present in the previous year (persistent), those that reactivated after vegetation regrowth (recurrent), and those that newly occurred. We also identified the area of recovery for each year if there was observed revegetation following a landslide event. To calculate the number and size of landslides, we converted raster maps into vector data using ArcGIS.

As the aggregated level, we attributed first occurrence, persistence, and recurrence for each pixel over the period 1992-2021 (Fig. 4). The first occurrence indicates the year when a landslide was initially observed. Since our study period is from 1992 to 2021, we can only identify landslides that occurred after 1992. The persistence metric measures the longest consecutive period, in years, during which a pixel was classified as a landslide scar. The recurrence metric captures the frequency of landslide reactivation. Additionally, we calculated the kernel density of recurrence and persistence against elevation and slope. The difference in kernel density signifies the landslide density that was either higher or lower than the background density of the topographical features (further details in Kincey et al. (2021)). We used R's *density* function for the kernel density analysis.

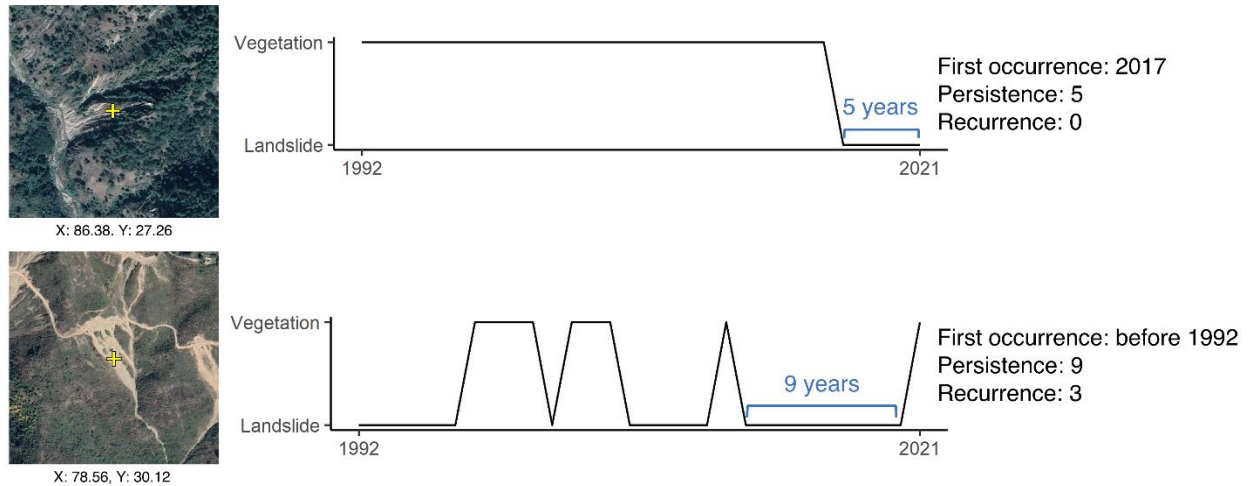


Fig. 4. Examples of first occurrence, persistence, and recurrence attributes at the pixel level.

## 4. Results

### 4.1 Persistent and recurrent landslides over 30 years

We found that on average, of the entire landslide area mapped each year, only 14% of this area had not been a landslide previously. Each year, 55-83% of the landslide area mapped was classified as persistent and 3-24% as reactivated (Fig. 5); over this timescale landslides therefore predominantly persist or reoccur in locations where they have occurred previously. The satellite imagery also shows many landslide areas experienced vegetation regrowth a year after the landslide event (27%). However, despite instances of quick recovery, more than 50% of the previously recovered areas experienced recurrent landslides after an average of 5.2 years (SD = 4.9 years).

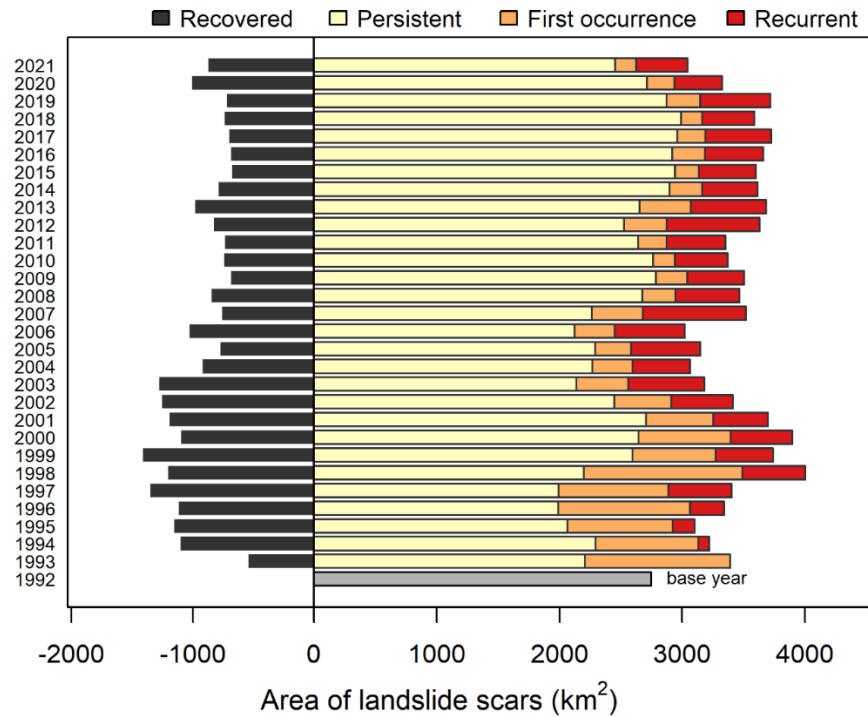


Fig. 5. Annual area estimate across 1992-2021. Recovered represents a landslide scar that was detected a year before but revegetated. Persistent scars are scars present in a previous year in the time series. First occurrence scars are those that were not previously detected in the study period. Recurrent scars are those that were detected previously, revegetated and then experienced a landslide again.

We observed the highest total area of landslides in 1998 (4,005 km<sup>2</sup>) and the lowest in 2006 (3,292 km<sup>2</sup>), representing 1.07% and 0.81 % of the ground surface respectively. Although the Himalaya's size makes it challenging to attribute the overall pattern to a single seismic or storm event, we observed a significant correlation between the temporal variation in the new landslide area and South Asian Summer Monsoon Index in July and August ( $p < 0.05$ ) (Li and Zeng, 2002), showing the effect of monsoon strength and its interannual variability. Furthermore, our

analysis showed an overall decreasing trend in the new landslide area over time, although this observation may be biased due to the longer historical record available for the later years in our analysis.

#### ***4.2 Geographical distribution of landslides and first occurrence***

We found highly heterogeneous trends in landslides across the Himalaya (Table 1; *Appendix Table S1*). Western India, which has the fastest population growth in the region, experienced the most rapid increase in the number and area of landslides, adding landslides at a rate of  $> 0.01\%$   $yr^{-1}$  of the ground surface area per year, with larger than average landslides ( $\sim 17,000\text{ m}^2$ ). Nepal exhibited the second-highest rate of change in landslide area ( $0.005\%$   $yr^{-1}$ ), which was notably increased following the 2015 Gorkha earthquake. The rate of change in Bhutan and Eastern India was still positive, but in comparative terms minimal ( $< 0.0001\%$   $yr^{-1}$ ). At this broad administrative scale, all parts of our study area have therefore experienced increased rates of landsliding over the study period.

Table 1. Total number and area of landslides by time period and region. For each period the average number and area of landslides are derived from annual data. Annual rates of change in landslide area ( $\% yr^{-1}$ ) are derived from simple ordinary least squares linear regression models for  $10\text{ km} \times 10\text{ km}$  cells over 1992 to 2020 and then averaged by region excluding cells without landslides.

Period	Country/Region			
<i>N of landslides</i>	Western India	Nepal	Bhutan	Eastern India
1992-1999	66536	78749	16406	83039
2000-2005	76364	81894	20547	82907

2006-2014	89082	69889	15213	72508
2015-2021	95171	82356	17387	70317
<i>Area of landslides (km<sup>2</sup>)</i>				
1992-1999	1232	1169	178	740
2000-2005	1379	1120	225	796
2006-2014	1541	1007	176	742
2015-2021	1460	1142	194	732
<i>Average size (m<sup>2</sup>)</i>				
1992-1999	18513	14840	10834	8915
2000-2005	18057	13680	10966	9600
2006-2014	17299	14412	11552	10235
2015-2021	15336	13861	11152	10412
Annual rate of change (% yr <sup>-1</sup> )	0.0133	0.0047	0.00008	0.00006

Furthermore, we captured highly heterogenous trends in landsliding even within the same country (Fig. 6). Notable higher rates of landslide area change were observed in Northern Bagmati (Nepal) the 2015 Mw 7.8 Gorkha earthquake (Fig. 6). Additionally, we identified another hotspot of increased landslide activity associated with intensive road development between 2014 and 2017 in Tehri Garhwal, Uttarakhand. Constructing new roads led to extensive landslides nearby the National Highway 7, as hillside along the already cultivated slope were cut (Fig. 6) (Kumar and Anbalagan, 2016). Extreme rainfall events in Western India in 2013 and subsequent years may also serve as another trigger (Martha et al., 2015; Pham et al., 2018). Interestingly, at this scale of analysis, the landslide impacts of road building are comparable in intensity to those associated with earthquakes. Conversely, we observed a declining landslide area in Karnali, the Mid-Western region of Nepal and in Sirmour in Himachal Pradesh, India. This decrease may involve a combination of afforestation and artifacts in high-elevation areas (Fig. 6). For example, the decrease in Sirmour was aligned with the increase in open forest cover, which doubled between 1997 and 2003 due to afforestation efforts after the 1986 ban on green felling in Himachal Pradesh and the 1993 forestry act across Nepal (Gupta 2007; Van Den Hoek et al. 2021). It is also plausible that some landslides persisted from before our analysis (i.e., pre-1992) and recovered during our study period, a factor we were unable to quantify.

### Annual rate of change in landslide area

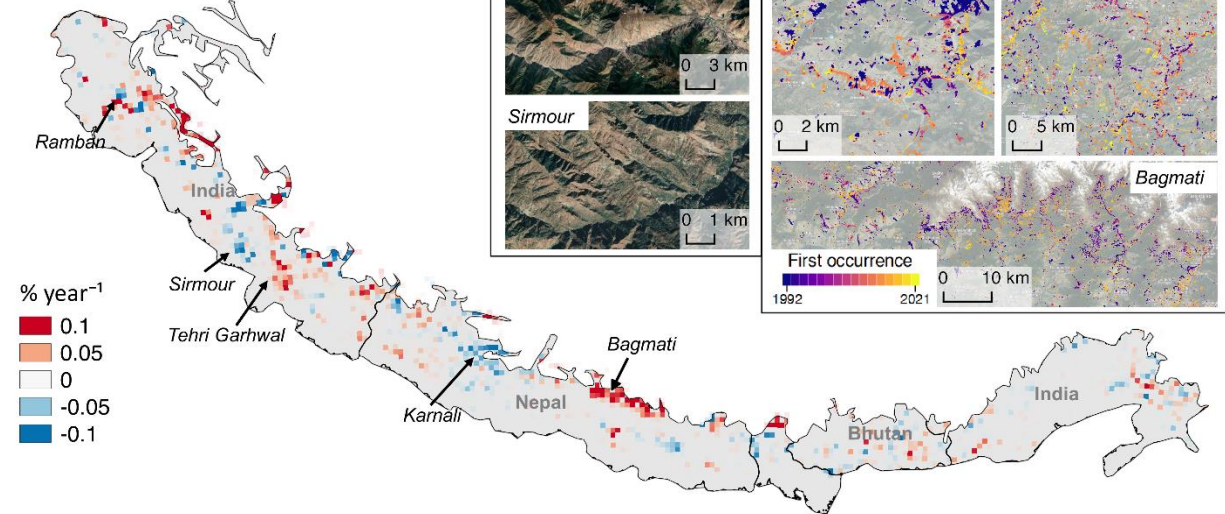


Fig. 6. Annual rate of change in landslide area ( $\% \text{ yr}^{-1}$ ) from 1992 to 2020 by fitting simple ordinary least squares linear regression models to timeseries data on landslide area for each  $10 \text{ km} \times 10 \text{ km}$  cell. Increasing cases are overlaid with the first occurrence layer, showing road-related increases in Tehri Garhwal and Ramban, as well as earthquake related increases in Bagmati. Decreasing cases present landscapes that experienced vegetation recovery (e.g., Sirmour (India)) and noise from glacial terrain (e.g., higher elevations in Karnali (Nepal)).

The calculation of first occurrence from our time-series results is a valuable tool for identifying triggering factors, revealing distinct regional heterogeneity (Fig. 7). In Western India, the areal landslide density of first occurrences decreased from 1.3% to 0.5% over the period 2006-2014 to 2015-2021. In contrast, Nepal's areal landslide density slightly increased from 0.42% to 0.47% across the same period. The disparity between Western India and Nepal could potentially be attributed to the impact of the 2005 Kashmir earthquake in Western India (Fig. 7A) and the 2015 Gorkha earthquake in Nepal (Fig. 7C). For comparison, the mean areal density of

landslides after the 2015 Gorkha earthquake was reported as 0.72% by Kincey et al. (2021) and 0.25% by Martha et al. (2017), and as 0.38% over the period 1998-2018 by Jones et al. (2021) in central-eastern Nepal. While we anticipated a lower areal density in our analysis due to our broader geographical scope and resolution limits on minimum detectable events, the eventual higher estimates are likely to be attributed to overestimation in high-elevation areas, which were excluded in the two reference studies.

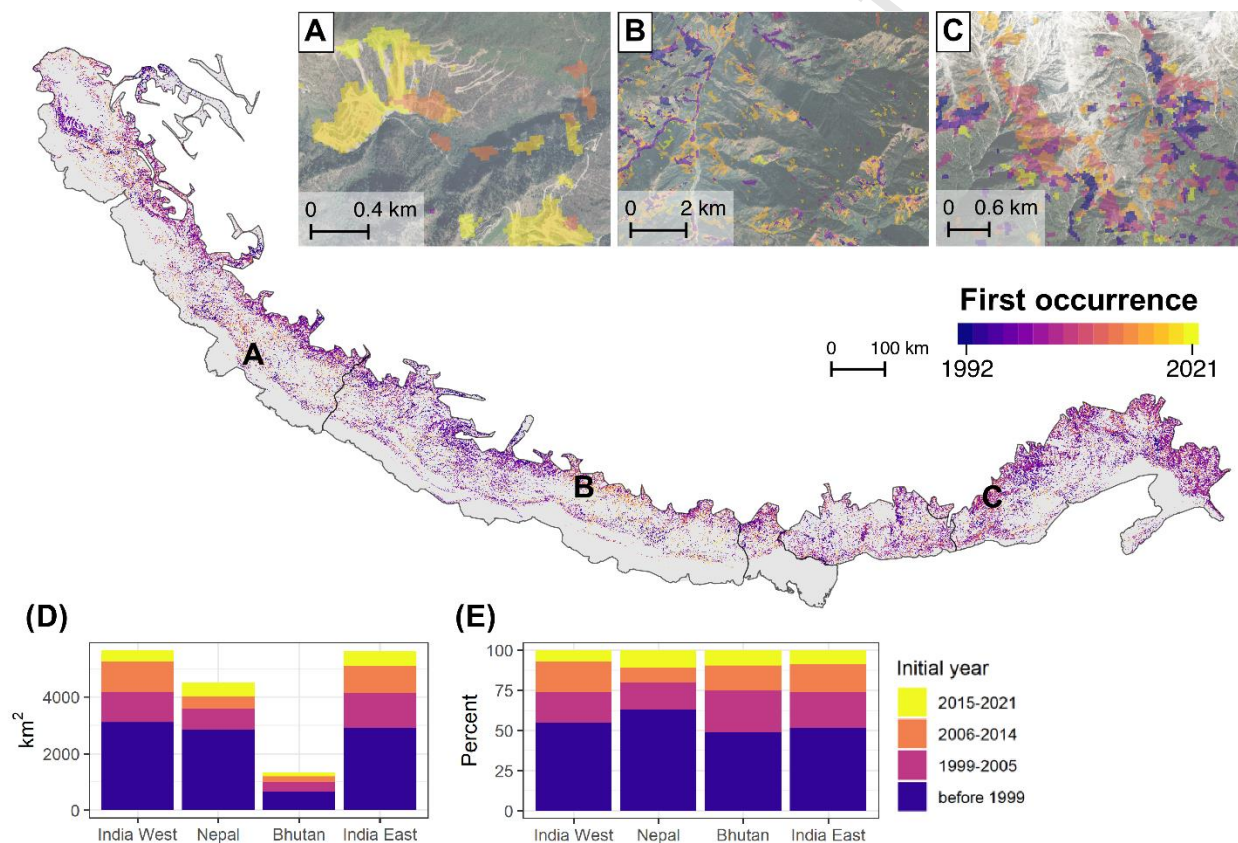


Fig. 7. First occurrence of landslides across the HKH. Inset maps (A) landslides triggered right after road construction in Tehri Garhwal, Uttarakhand in 2020, (B) substantial increases in landslides after the 2015 Gorkha Earthquake in Bagmati, north of Kathmandu, and (C) noisy results on glacial terrain in Eastern India. Inset graphs (D) total area and (E) percentage of first occurrences by region and period.

### ***4.3 Cumulative landslide persistence, recurrence and topography***

Results stacking our 30-year timeseries into per pixel counts of landslide occurrence showed that a landslide pixel's longest continuous mapped period (i.e., persistence) was on average 4.7 years before full recovery, with a standard deviation of 6.4 years. Breaking the frequency of landsliding per pixel down, about 39% of the landslide area revegetated within two years, 50% took two to ten years, and 11% over a decade, including 5% over two decades (Fig. 8). This means that 89% of our mapped landslide scar area (equivalent to 14767 km<sup>2</sup>) persisted for a sub-decadal period. Despite this 5% remained longer, representing 850 km<sup>2</sup> of the landslide scars within the Himalayas, that took at least two decades to revegetate. Although a significant portion of the mapped landslide area revegetated, 43% of our mapped landslide area then experienced further landsliding or recurrence, and 22% of the landslide area experienced at least two further episodes of landslides in the time series, including 1.5% which experienced landslides in at least five discrete episodes.

The spatial distribution of landslide persistence and recurrence showed evolutionary characteristics of individual landslides at the local level and revealed regional disparities. At the local level, the peripheral area of a landslide recovered sooner than the central area whereby landslide footprint constricted through time (Fig. 8A, B). Larger landslides tended to persist longer, and landslides in higher relief areas reoccurred more frequently (Fig. 8C). Over the Himalaya, landslide persistence was higher in the west, with an average recovery time of 6 years across Western India and Nepal, compared to 3 years for Bhutan and Eastern India. Recurrent landslides are more prevalent in Western India (90<sup>th</sup> percentile: reoccurred 2 times) than other Himalayan regions (90<sup>th</sup> percentile: 1 time) (Fig. 8).

Persistent landslides were observed to occur on steeper slopes and lower elevations than those which were more short-lived in the landscape (Fig. 9). Landslides that persisted for four years or longer were more likely to occur on steep slopes between 40 and 55°, suggesting recovery is impeded by topography. Landslides that persisted for four years or more are also more likely to occur at middle elevations in our study area, below 3000 m, compared to shorter-term landslides. Across all degrees of persistence and recurrence, landslides occurred much less frequently at lower (< 2,000 m) elevations, despite this representing 63% of our HKH study area.

Landslide recurrence varied in relation to slope and elevation (Fig. 9). Higher recurrence rates were observed on steeper slopes, peaking at 44°, indicating again the influence of shear stresses in controlling reactivation. Landslides with higher recurrence rates were also found to occur at higher elevations. The distribution of landslide scars with low persistence and high recurrence significantly increased above 3,000 m. However, these short-term observations could be influenced by false positives resulting from variable snow cover, shadow effects, and loose debris.

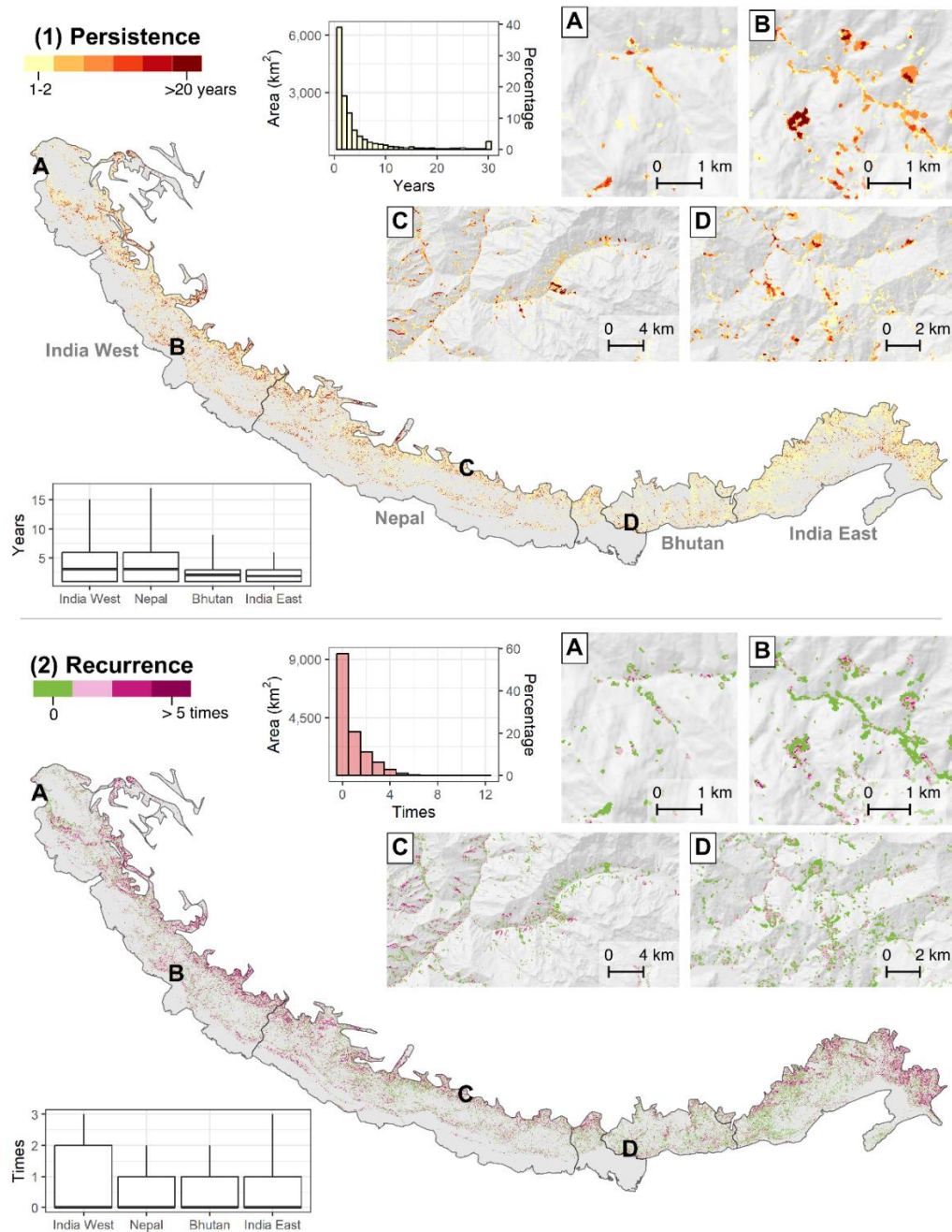


Fig. 8. Geographical distribution of landslide persistence and recurrence. The histogram illustrates the overall frequency, and the box plot displays region-specific statistics. Insets: (A) earthquake-triggered landslides in Kashmir 2005, (B) recurrent landslides (three clusters) near roadsides, (C) a wide temporal spectrum of landslide clusters, and (D) heterogeneity of persistence within landslide objects.

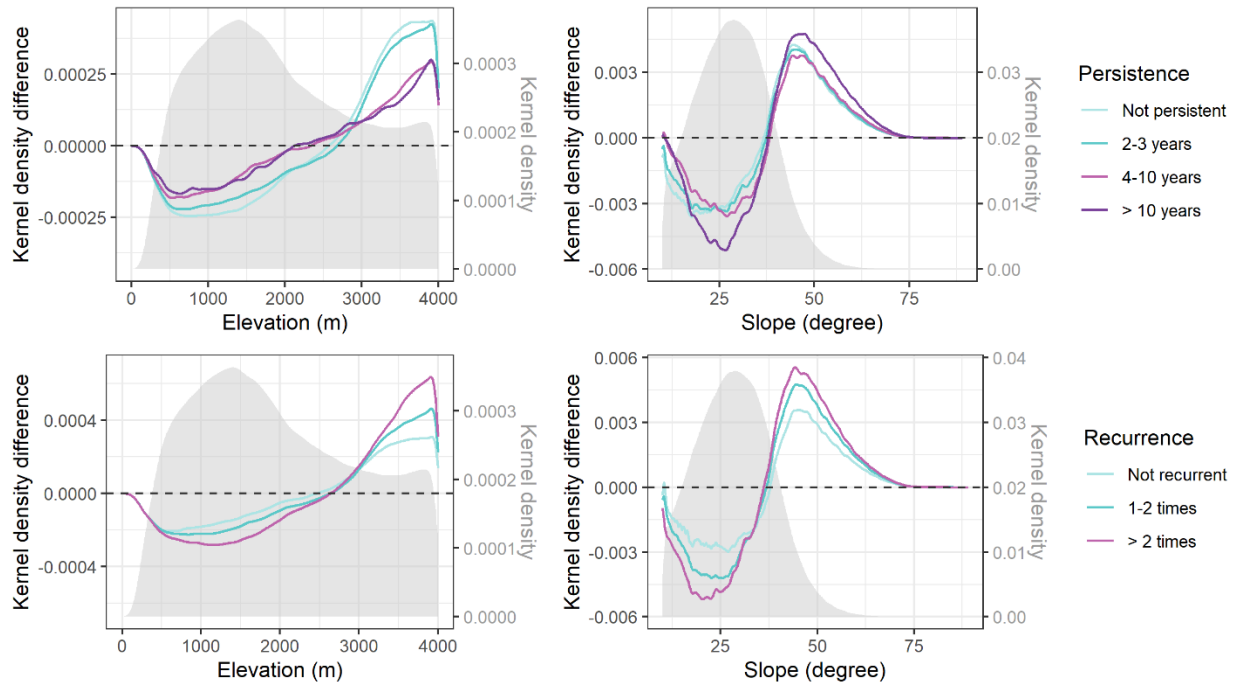


Fig. 9. Topographic controls on landslide persistence and recurrence, displayed as difference in kernel density values relative to the density distribution from the overall study area. The area under the curve of a kernel density plot within a specific range of values can be interpreted as the probability of this range of values. Slopes below 10 degrees were excluded as these areas are unlikely to experience landslides (Meunier et al., 2008).

## 5. Validating the location and timing of landslides

### *5.1 Visually interpreted accuracy: topography, nightlights, and multi-year data*

We initiated the accuracy assessment by evaluating various input combinations. Including Digital Elevation Model data resulted in a notable improvement in accuracy compared to using Landsat imagery alone, with the F1 score increasing from 76.9% to 82.8% ( $p < 0.05$ ).

Additionally, incorporating nightlight data further enhanced the precision (user's accuracy) significantly ( $p < 0.05$ ). This enhancement is likely attributed to the ability of nightlights to reduce false positive landslides associated with clustered settlements that are observable in nightlight data with a resolution of 500 m. This complements earlier landslide mapping using nightlight data (Chen et al., 2019), showing that it is helpful for machine learning classification in rural developing countries with generally lower luminosity.

In terms of multi-year data, using two-year data for training the model yielded higher accuracy compared to utilizing only one-year data. However, there was no significant difference in accuracy when comparing two-year and three-year data (Table 2). Overall, the combination of daytime imagery, nighttime data, and the DEM, along with two years of training data, resulted in the highest accuracy.

Table 2. Accuracy comparison for different remote sensing inputs by multi-sensor data (Landsat, DEM, nightlight) and the number of years. Standard error was measured at  $p < 0.05$  from 20 iterations with resampling. The accuracy is assessed by the visual interpretation of historical time-series data on Google Earth.

Multitemporal data	Overall accuracy	Precision (UA)	Recall (PA)	F1
Landsat	$94.2 \pm 0.8$	$76.9 \pm 4.1$	$77 \pm 5.5$	$76.9 \pm 3.5$
Landsat + DEM	$95.7 \pm 0.7$	$82.6 \pm 3.4$	$83 \pm 3.7$	$82.8 \pm 2.9$
Landsat + DEM + Nightlight	$95.9 \pm 0.7$	$83.7 \pm 2.6$	$83.3 \pm 4.5$	$83.5 \pm 3$
Input features				
One year	$95.6 \pm 1.9$	$82.1 \pm 3.9$	$82.3 \pm 14.8$	$82.1 \pm 9.2$
Two years	$95.9 \pm 0.7$	$83.7 \pm 2.6$	$83.3 \pm 4.5$	$83.5 \pm 3$
Three years	$95.8 \pm 0.6$	$83.5 \pm 2.5$	$83.2 \pm 3.7$	$83.3 \pm 2.6$

### ***5.2 Reported landslide events across the Himalaya***

Our time-series mapping of landslides detected events with timing and locations proximal to 94% of the landslide events recorded in both the Global Fatal Landslide Dataset and the Global Landslide Catalog, ranging from 84% to 100% from 2005 to 2017 (Fig. 10). The lowest detection rate, 84% in 2006, was primarily due to false reports, as all six false negatives were located in plain areas with flat agricultural fields, situated at elevations below 150 m.

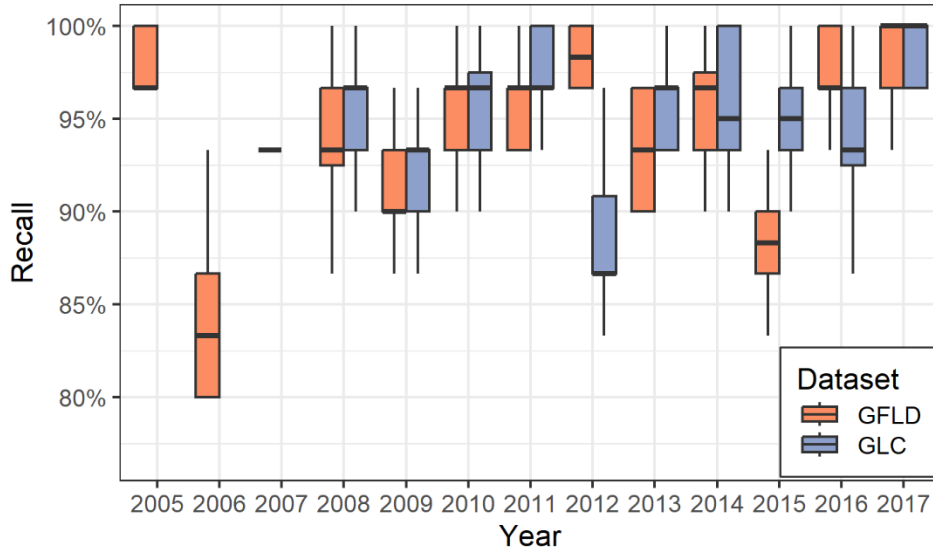


Fig. 10. Detection rate measured as recall score for reported landslide events across the HKH region between 2005 and 2017. The report-based datasets include NASA's Global Landslide Catalog and the Global Fatal Landslide Database. The low recall value (84%) for 2006 was affected by mis-reported events (five among six undetected events were reported at lowland – elevation < 150 m).

### 5.3 Ward-level correlation

At the ward level, our predictions showed a strong correlation ( $R^2 > 0.8$ ) with the reference maps across all four years between 2016 and 2019 for the total landslide area, landslide areal density, and the number of mapped landslide objects (Fig. 11). Correlations for the training years (i.e., 2016 and 2017) were higher than for the other years ( $R^2$  training: 0.88-0.95 vs. out-of-sample: 0.83-0.87). Overestimation was more likely to occur in higher-elevation regions, with Chum Nubri, a ward where 80% of land is above 3000 m, having the highest overestimation. The correlation for object number was slightly lower than that for area and areal density among the

three assessments, which could be attributed to Landsat's 30-m resolution blurring the boundaries between neighboring landslide objects.

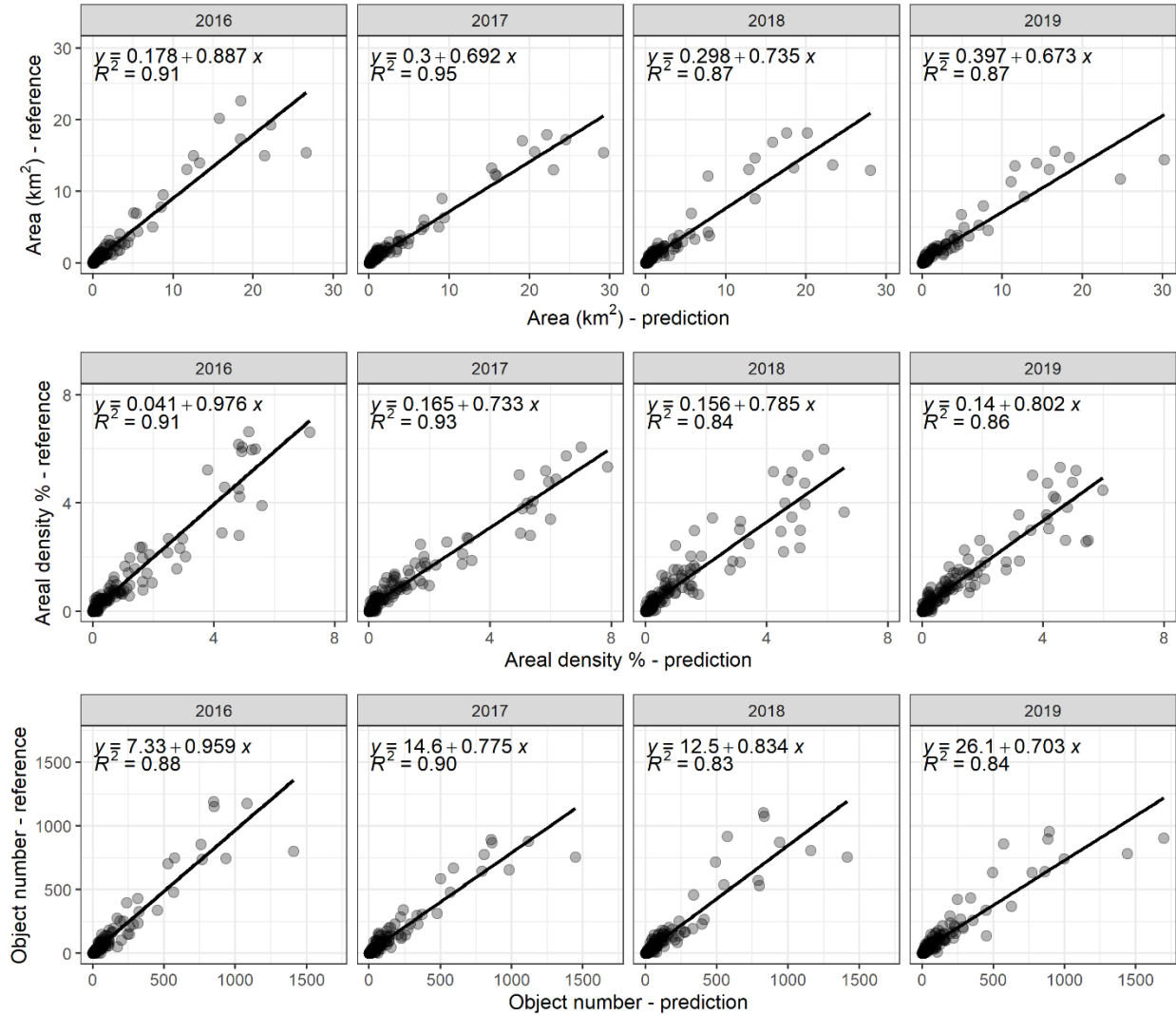


Fig. 11. Predicted landslide area, areal density, and object number at the ward level in comparison with visually interpreted reference map (Kincey et al. 2021).

## 6. Discussion

### *6.1 Multi-temporal landslide mapping at scale*

The ability to generate landslide inventory data at this scale has previously proven a bottleneck in systematic landslide mapping, meaning that large scale controls on landslides, and their variability across space and through time, have remained elusive. The methodology presented here allows for generating a continuous 30-year inventory that has a wide range of potential uses. The spatial coverage in this study is unique, including over 265,000 landslides across North India (~165,500), Nepal (~82,400), and Bhutan (~17,400) that encompass broadly comparable physiographic characteristics.

The persistence of these landslides is highly heterogeneous, with 39% (6470 km<sup>2</sup>) recovered within two years and 11% (850 km<sup>2</sup>) over a decade. The distribution of recovery time over the Himalaya was faster than after the 2005 Kashmir earthquake, which shows post-earthquake landslide area only recovered 15% within five years and 80% after eleven years. This is possibly due to our larger study area than the Kashmir case study (only focusing on part of Northwestern India) and rainfall-triggered landslides may recover faster than landslides triggered by a major earthquake (Wu and Lin, 2021). More research is needed on the relative persistence of landslides as a function of the preconditioning and triggering factors. Comparing landslide persistence in the Himalaya with local cases in other regions, we find that the vegetation recover rates were very similar to the vegetation recovery after the 2008 Wenchuan earthquake (39% recovered within two years, and 89% within a decade) (Yunus et al., 2020; Chen et al., 2021) and after Typhoon Morakot (80% after 8 years) (Wu, 2021), but slower than after the 1999 Chi-Chi earthquake (recovered 50% within two years and 90% over six years) (Lin et al., 2005).

Faster vegetation recovery has been found related to lower elevations (Yang et al., 2018; Yunus et al., 2020; Chen et al., 2021; Kinsey et al., 2021; Saito et al., 2022), shallower slopes (Yunus et al., 2020; Chen et al., 2021; Kinsey et al., 2021), shady slope aspects with higher soil moisture (Lin et al., 2005; Saito et al., 2022), sunny slope aspects (Yunus et al., 2020), slope aspects away from the direction of monsoonal rains (Kinsey et al., 2021), El Niño Southern Oscillation (Wu and Lin, 2021), and for smaller landslide sizes (Wu, 2021). Frequent reactivation has also been related to precipitation (Shou et al., 2011; Chen et al., 2021) and steeper slopes (Chen et al., 2021). While these studies are mostly based on watershed-scale assessments, our results provide an opportunity to evaluate these controls over a wider gradient.

## **6.2 Future research: four emerging directions**

Our study provides a comprehensive dataset of recurrent and persistent landsliding that enables progress to be made in our understanding of landscape-scale hazard evolution. This approach moves beyond typical studies that are limited by administrative boundaries or small-scale event-based assessments and allows four key questions at mountain range scale to be tackled. First, the scale of this dataset covers a variety of covariates and thus allows for analyzing complex anthropogenic and climatic drivers of *landscape evolution*. Looking at patterns of landsliding at this scale provides opportunities to detect the impact of (1) discrete events (e.g., earthquakes and cloudbursts), (2) changing human activities, which vary considerably across the HKH, and (3) potentially the impact of climatic changes over decadal timescales, on landslide occurrence and their aggregate impact on erosion, denudation and landscape evolution rates. These data also provide a useful temporal baseline against which to test ideas around the long-term interplay of erosion and orogenesis in active mountain ranges.

Second, the time-series landslide information has the potential to improve landslide *susceptibility models*. Multi-temporal information is likely to capture a greater and more long-term representative range of landslide triggering conditions (Jones et al. 2021). Wide spatial coverage, on the other hand, provides a greater variety of topographical, geological, and hydrological conditions to further improve susceptibility models. We also know that in general terms 'landslides follow landslides' (Samia et al., 2017), but the degree to which landslides occur at specific individual locations, and how this varies through time and space, has not been previously demonstrated at scale. Here we show that 43% of landslides occur in locations of previous landslides within our 30-year timescale. The annual resolution of the data also, excitingly, allows us to show the decreasing rate of occurrence through time, which provides insight on over what timescale all susceptible areas within a mountain landscape could be expected to fail and reset, opening up a new dimension to landslide susceptibility models and maps.

Third, recurrence and persistence can inform *engineering strategies* and policies. A key challenge in the mitigation of landslides in the HKH is that many are of a scale that renders them difficult to engineer to a point of stability. As a result, developing mitigation strategies that are cognizant of the time over which any individual landslide is likely to remain active has potential value in allocating resources in a more informed manner. The recurrence of landslides has been identified in specific locations in our study, and it may be that these are too costly or complex to mitigate. The transboundary nature of recurrent landslide hazards and the sediment that they release also holds implications for risk sensitive location of infrastructure development, such as hydroelectric power.

Fourth, the historical information regarding landslides provides insight into the *effectiveness of policy interventions*. For example, the long-term implications of significant investment in infrastructure, such as the Himalayan rural road network, remain largely anecdotal due to the lack of high-resolution landslide data at the scale presented here. Our results have the potential to identify key learning around, for example, the physiographic conditions that are conducive to safe and sustainable rural road construction, and those which are not. For example, the recovery of the landscape after road construction can indicate whether the construction is successful. Similar insight on the short- and long-term implications of complex social and political changes may also become apparent, including the often cited but rarely evidenced impacts of terrace abandonment (Tarolli et al., 2021), civil war and informal settlements (Petley et al., 2007), and changes associated with regulation around conversation (e.g., community forestry groups) (Dhungana et al., 2020). We also have the potential to identify the relative significance of the covariates of risk through time, and hence to unpick the costs and benefits of risk reduction policies that focus on reducing hazard versus tackling exposure and vulnerability.

### ***6.3 Machine learning achievement, complexity and uncertainty***

Built upon a visually interpreted training data in Nepal, our model captured > 94% of the reported landslide events across the Himalayan region including Bhutan and India, which demonstrate the model's generalizability. This is a major strength of the machine learning methodology: it amplifies the value of visually interpreted data and enables the identification of persistent and recurrent landslides across an area > ten times larger than the training data. Furthermore, it allows for the tracing of landslides back to 1992, a period predating the availability of the training data in 2016. Based on the publicly available datasets, Landsat optical

imagery, nighttime lights, and the digital elevation model, the methodology has potential to identify persistent and recurrent landslides in other mountain areas around the world. The model based on convolutional neural networks achieved precision and recall rates exceeding 83% in independent test sites, which is superior to earlier Landsat-based landslide mapping at national and sub-national scales using other algorithms (32-86%) (Yu and Chen, 2017; Chen et al., 2019) and is comparable in accuracy to studies using object-based imagery analysis based on high resolution images (2-10 m) (69-87%) (Martha et al., 2010; Stumpf and Kerle, 2011; Amatya et al., 2021).

Nevertheless, this model is not without uncertainty and bias arising from model assumptions, limited spatiotemporal resolution, and inherent landscape variability. The spatial resolution of 30 m can be particularly challenging in areas which suffer from spectral similarity between landslides and other land covers (Kincey et al., 2021), including gravels and talus at higher elevations above tree line, landslides occurring within built-up areas, and landslides smaller than the minimum detectable area (900 m<sup>2</sup>) (*Appendix Fig. S1*). As multi-temporal elevation data over the study region is not available, we cannot capture changes in stream course over the years, and artifacts from streams and riverbeds are present in our landslide output. Similar challenges arise in identifying landslides from shadows in gullies and on north-facing slopes, where fieldwork is necessary to observe landslides.

#### ***6.4 Strengths and limitations compared to other RS-based methods***

Other current approaches for generating multi-temporal inventories include manual mapping, vegetation index-based metrics (Behling et al., 2014; Scheip and Wegmann, 2021; Milledge et al., 2022), and object-based imagery analysis (OBIA) and machine learning (Li et al., 2015;

Amatya et al., 2021; Ghorbanzadeh et al., 2022). Our CNN-based deep learning approach offers distinct advantages. First, CNN-based deep learning requires the least expert knowledge while enabling the model to automatically learn from spatial and spectral information in training data, without the need for segmentation and rulesets as required by OBIA. Second, CNN-based methods demonstrate enhanced landslide detection capabilities, reducing the salt-and-pepper effect through their utilization of spatial information, which contrasts with vegetation-based metrics or pixel-based machine learning models that rely solely on spectral information (Liu et al., 2022). Thirdly, the proposed approach is particularly advantageous for large-scale mapping given its automatic nature. While vegetation-based metrics offer quick insights into vegetation changes, their applicability is constrained in regions with cloud cover like the Himalaya, as they hinge on temporal differences (Milledge et al., 2022).

However, the major limitation of the CNN-based deep learning lies in the demand for a large and representative training dataset – how the landslide labels related to the spatial patterns of surface reflectance, nightlights, elevation, and slope. Thus, the model's performance might decrease if applied to other regions where the optical and topographical features of landslides and non-landslide areas are very different from the Himalaya. Given its reliance on spatial information, complete landslide objects in polygon format are indispensable for preparing training data, unlike pixel-based machine learning models which can utilize discrete point data. The increasing popularity of open science has led to more regional landslide studies publishing their manually mapped datasets (e.g., Jones et al., 2021; Kinsey et al., 2021), thus fortifying the potential of leveraging these datasets to facilitate CNN-based deep learning approaches.

## 7. Conclusions

We are in an era where petabytes of images recorded by satellites every year are publicly available. Their potential benefits for science and society are revolutionized through the alignment of artificial intelligence, which has reduced human labor for identifying risks at large scales. Our findings draw three main conclusions:

First, it is possible to use data from a small area to train a machine learning model for a region ten times larger if they have similar geography. We used a dataset in Central Nepal to map out landslides over the Himalaya, successfully capturing 94% of the reported landslides in the region. This mountain range scale, exceeding previous catchment or even national administrative boundary scales, has the potential to enhance studies in landscape evolution, susceptibility models, engineering strategies, transboundary collaboration, and policy validation, all together working towards sustainable mountain development.

Second, the current trend of landslide risks in the Himalaya exhibits several clusters, including patterns related to road construction, climate, and recent seismic events. Future research using this large-scale multitemporal dataset will be essential for disaggregating these various sources of risk and for aiding in mitigation strategies.

Third, the lifecycle of landslides proves to be highly dynamic. The methodology allows for the identification of persistent and recurrent landslides, particularly at elevations below 3,000 m, where the contrast between vegetation and landslides is more visible. The time dimension regarding recurrent and persistent landslides can be instrumental in alerting and informing awareness of cascading effects to vulnerable communities. While this study focused on

landslides, the power of combined earth observation and artificial intelligence can be harnessed for other types of hazards and their intersections. It is our hope that open science will further accelerate this advancement.

### Author contributions

All authors conceptualized the research; T.K.C., M.K., and N.R. designed the methods; T.K.C. performed the research; and all authors wrote the manuscript.

### Acknowledgments

We thank Shelby Warrington, Andrew West, and Nathan Nicholas for helping prepare the data set. This research was supported by NASA's LCLUC grant NNX17AH98G, the Gaylord Donnelley Environmental Postdoctoral Fellowship at Yale, the UKRI-DFID SHEAR program (201844-112), and by a grant from the Global Challenges Research Fund Multi-Hazard and Systemic Risk programme for the 'Sajag-Nepal' project (NE/T01038X/1).

### Data availability statement

The satellite images, training data, and multi-temporal landslide inventory, and recurrence, persistence, and first occurrence maps are available on GitHub (<https://github.com/karenthchen/Persistent-recurrent-landslide-Himalaya>).

### References

- Amatya, P., Kirschbaum, D., Stanley, T., & Tanyas, H. (2021). Landslide mapping using object-based image analysis and open source tools. *Engineering geology*, 282, 106000.
- Behling, R., Roessner, S., Golovko, D., & Kleinschmit, B. (2016). Derivation of long-term spatiotemporal landslide activity—A multi-sensor time series approach. *Remote Sensing of Environment*, 186, 88-104.
- Behling, R., Roessner, S., Kaufmann, H., & Kleinschmit, B. (2014). Automated spatiotemporal landslide mapping over large areas using rapideye time series data. *Remote Sensing*, 6, 8026-8055.
- Chen, M., Tang, C., Wang, X., Xiong, J., Shi, Q., Zhang, X., Li, M., Luo, Y., Tie, Y., & Feng, Q. (2021). Temporal and spatial differentiation in the surface recovery of post-seismic landslides in Wenchuan earthquake-affected areas. *Ecological Informatics*, 64, 101356.
- Chen, T.-H.K., Pandey, B., & Seto, K.C. (2023). Detecting subpixel human settlements in mountains using deep learning: A case of the Hindu Kush Himalaya 1990–2020. *Remote Sensing of Environment*, 294, 113625.
- Chen, T.-H.K., Prishchepov, A.V., Fensholt, R., & Sabel, C.E. (2019). Detecting and monitoring long-term landslides in urbanized areas with nighttime light data and multi-seasonal Landsat imagery across Taiwan from 1998 to 2017. *Remote Sensing of Environment*, 225, 317-327.
- Dhungana, N., Silwal, N., Upadhaya, S., Khadka, C., Regmi, S.K., Joshi, D., & Adhikari, S. (2020). Rural coping and adaptation strategies for climate change by Himalayan communities in Nepal. *Journal of Mountain Science*, 17, 1462-1474.
- Fan, X., Domènech, G., Scaringi, G., Huang, R., Xu, Q., Hales, T.C., Dai, L., Yang, Q., & Francis, O. (2018).

- Spatio-temporal evolution of mass wasting after the 2008 M w 7.9 Wenchuan earthquake revealed by a detailed multi-temporal inventory. *Landslides*, 15, 2325-2341.
- Froude, M.J., & Petley, D.N. (2018). Global fatal landslide occurrence from 2004 to 2016. *Natural Hazards and Earth System Sciences*, 18, 2161-2181.
- Gariano, S.L., & Guzzetti, F. (2016). Landslides in a changing climate. *Earth-Science Reviews*, 162, 227-252.
- Ghorbanzadeh, O., Blaschke, T., Gholamnia, K., Meena, S.R., Tiede, D., & Aryal, J. (2019). Evaluation of different machine learning methods and deep-learning convolutional neural networks for landslide detection. *Remote Sensing*, 11, 196.
- Ghorbanzadeh, O., Shahabi, H., Crivellari, A., Homayouni, S., Blaschke, T., & Ghamisi, P. (2022). Landslide detection using deep learning and object-based image analysis. *Landslides*, 19, 929-939.
- He, K., Zhang, X., Ren, S., & Sun, J. (2016). Deep residual learning for image recognition. In *Proceedings of the IEEE conference on computer vision and pattern recognition* (pp. 770-778)
- Hovius, N., Meunier, P., Lin, C.-W., Chen, H., Chen, Y.-G., Dadson, S., Horng, M.-J., & Lines, M. (2011). Prolonged seismically induced erosion and the mass balance of a large earthquake. *Earth and Planetary Science Letters*, 304, 347-355.
- Jones, J.N., Boulton, S.J., Stokes, M., Bennett, G.L., & Whitworth, M.R. (2021). 30-year record of Himalaya mass-wasting reveals landscape perturbations by extreme events. *Nature communications*, 12, 6701.
- Jpl, N. (2020). NASADEM Merged DEM Global 1 arc second V001. *NASA EOSDIS Land Processes DAAC*
- Kincey, M.E., Rosser, N.J., Densmore, A.L., Robinson, T.R., Shrestha, R., Singh Pujara, D., Horton, P., Swirad, Z.M., Oven, K.J., & Arrell, K. (2023). Modelling post-earthquake cascading hazards: Changing patterns of landslide runout following the 2015 Gorkha earthquake, Nepal. *Earth Surface Processes and Landforms*, 48, 537-554.
- Kincey, M.E., Rosser, N.J., Robinson, T.R., Densmore, A.L., Shrestha, R., Pujara, D.S., Oven, K.J., Williams, J.G., & Swirad, Z.M. (2021). Evolution of coseismic and post-seismic landsliding after the 2015 Mw 7.8 Gorkha earthquake, Nepal. *Journal of Geophysical Research: Earth Surface*, 126, e2020JF005803.
- Kingma, D.P., & Ba, J. (2014). Adam: A method for stochastic optimization. *arXiv preprint arXiv:1412.6980*
- Kirschbaum, D.B., Adler, R., Hong, Y., Hill, S., & Lerner-Lam, A. (2010). A global landslide catalog for hazard applications: method, results, and limitations. *Natural Hazards*, 52, 561-575.
- Kumar, R., & Anbalagan, R. (2016). Landslide susceptibility mapping using analytical hierarchy process (AHP) in Tehri reservoir rim region, Uttarakhand. *Journal of the Geological Society of India*, 87, 271-286.
- Lee, E.M., & Jones, D.K. (2023). *Landslide risk assessment*. ICE publishing.
- Lehner, B., Verdin, K., & Jarvis, A. (2008). New global hydrography derived from spaceborne elevation data. *Eos, Transactions American Geophysical Union*, 89, 93-94.
- Li, J., & Zeng, Q. (2002). A unified monsoon index. *Geophysical Research Letters*, 29, 115-111-115-114.
- Li, X., Cheng, X., Chen, W., Chen, G., & Liu, S. (2015). Identification of forested landslides using LiDAR data, object-based image analysis, and machine learning algorithms. *Remote Sensing*, 7, 9705-9726.
- Lin, C.-H., & Lin, M.-L. (2015). Evolution of the large landslide induced by Typhoon Morakot: A case study in the Butangbunasi River, southern Taiwan using the discrete element method. *Engineering geology*, 197, 172-187.
- Lin, W.-T., Chou, W.-C., Lin, C.-Y., Huang, P.-H., & Tsai, J.-S. (2005). Vegetation recovery monitoring and assessment at landslides caused by earthquake in Central Taiwan. *Forest Ecology and Management*, 210, 55-66.
- Liu, R., Yang, X., Xu, C., Wei, L., & Zeng, X. (2022). Comparative study of convolutional neural network and conventional machine learning methods for landslide susceptibility mapping. *Remote Sensing*, 14, 321.
- Mansour, M.F., Morgenstern, N.R., & Martin, C.D. (2011). Expected damage from displacement of slow-moving slides. *Landslides*, 8, 117-131.
- Marc, O., Hovius, N., Meunier, P., Uchida, T., & Hayashi, S.i. (2015). Transient changes of landslide rates after earthquakes. *Geology*, 43, 883-886.
- Martha, T.R., Kerle, N., Jetten, V., van Westen, C.J., & Kumar, K.V. (2010). Characterising spectral, spatial and

- morphometric properties of landslides for semi-automatic detection using object-oriented methods. *Geomorphology*, *116*, 24-36.
- Martha, T.R., Roy, P., Govindharaj, K.B., Kumar, K.V., Diwakar, P., & Dadhwal, V. (2015). Landslides triggered by the June 2013 extreme rainfall event in parts of Uttarakhand state, India. *Landslides*, *12*, 135-146.
- Martha, T.R., Roy, P., Mazumdar, R., Govindharaj, K.B., & Kumar, K.V. (2017). Spatial characteristics of landslides triggered by the 2015 M w 7.8 (Gorkha) and M w 7.3 (Dolakha) earthquakes in Nepal. *Landslides*, *14*, 697-704.
- Meena, S.R., & Tavakkoli Piralilou, S. (2019). Comparison of earthquake-triggered landslide inventories: a case study of the 2015 Gorkha earthquake, Nepal. *Geosciences*, *9*, 437.
- Meunier, P., Hovius, N., & Haines, J.A. (2008). Topographic site effects and the location of earthquake induced landslides. *Earth and Planetary Science Letters*, *275*, 221-232.
- Milledge, D.G., Bellugi, D.G., Watt, J., & Densmore, A.L. (2022). Automated determination of landslide locations after large trigger events: advantages and disadvantages compared to manual mapping. *Natural Hazards and Earth System Sciences*, *22*, 481-508.
- Muñoz-Torrero Manchado, A., Allen, S., Ballesteros-Canovas, J.A., Dhakal, A., Dhital, M.R., & Stoffel, M. (2021). Three decades of landslide activity in western Nepal: new insights into trends and climate drivers. *Landslides*, *18*, 2001-2015.
- Petley, D.N., Hearn, G.J., Hart, A., Rosser, N.J., Dunning, S.A., Oven, K., & Mitchell, W.A. (2007). Trends in landslide occurrence in Nepal. *Natural Hazards*, *43*, 23-44.
- Pham, B.T., Prakash, I., Jaafari, A., & Bui, D.T. (2018). Spatial prediction of rainfall-induced landslides using aggregating one-dependence estimators classifier. *Journal of the Indian Society of Remote Sensing*, *46*, 1457-1470.
- Reichenbach, P., Rossi, M., Malamud, B.D., Mihir, M., & Guzzetti, F. (2018). A review of statistically-based landslide susceptibility models. *Earth-Science Reviews*, *180*, 60-91.
- Robinson, T.R., Rosser, N., & Walters, R.J. (2019). The spatial and temporal influence of cloud cover on satellite-based emergency mapping of earthquake disasters. *Scientific Reports*, *9*, 12455.
- Saito, H., Uchiyama, S., & Teshirogi, K. (2022). Rapid vegetation recovery at landslide scars detected by multitemporal high-resolution satellite imagery at Aso volcano, Japan. *Geomorphology*, *398*, 107989.
- Samia, J., Temme, A., Bregt, A., Wallinga, J., Guzzetti, F., Ardizzone, F., & Rossi, M. (2017). Do landslides follow landslides? Insights in path dependency from a multi-temporal landslide inventory. *Landslides*, *14*, 547-558.
- Scheip, C.M., & Wegmann, K.W. (2021). HazMapper: a global open-source natural hazard mapping application in Google Earth Engine. *Natural Hazards and Earth System Sciences*, *21*, 1495-1511.
- Shen, P., Zhang, L.M., Fan, R., Zhu, H., & Zhang, S. (2020). Declining geohazard activity with vegetation recovery during first ten years after the 2008 Wenchuan earthquake. *Geomorphology*, *352*, 106989.
- Shou, K., Hong, C., Wu, C., Hsu, H., Fei, L., Lee, J., & Wei, C. (2011). Spatial and temporal analysis of landslides in Central Taiwan after 1999 Chi-Chi earthquake. *Engineering geology*, *123*, 122-128.
- Stumpf, A., & Kerle, N. (2011). Object-oriented mapping of landslides using Random Forests. *Remote Sensing of Environment*, *115*, 2564-2577.
- Tarolli, P., Pijl, A., Cucchiaro, S., & Wei, W. (2021). Slope instabilities in steep cultivation systems: Process classification and opportunities from remote sensing. *Land Degradation & Development*, *32*, 1368-1388.
- Tehrani, F.S., Calvello, M., Liu, Z., Zhang, L., & Lacasse, S. (2022). Machine learning and landslide studies: recent advances and applications. *Natural Hazards*, *114*, 1197-1245.
- Temme, A., Guzzetti, F., Samia, J., & Mirus, B.B. (2020). The future of landslides' past—a framework for assessing consecutive landsliding systems. *Landslides*, *17*, 1519-1528.
- Tiwari, P.C., Tiwari, A., & Joshi, B. (2018). Urban growth in Himalaya: understanding the process and options for sustainable development. *Journal of Urban and Regional Studies on Contemporary India*, *4*, 15-27.
- United States Geological Survey. (2020). Landsat Enhanced Thematic Mapper Plus (ETM+) Collection 2 Level 2

- Data Format Control Book. <https://www.usgs.gov/media/files/landsat-7-etm-collection-2-level-2-data-format-control-book>
- Wu, C.-H. (2021). Evaluating the landslide stability and vegetation recovery: Case studies in the Tsengwen reservoir watershed in Taiwan. *Water*, *13*, 3479.
- Wu, C., & Lin, C. (2021). Spatiotemporal hotspots and decadal evolution of extreme rainfall-induced landslides: Case studies in southern Taiwan. *Water*, *13*, 2090.
- Yang, W., Qi, W., & Zhou, J. (2018). Decreased post-seismic landslides linked to vegetation recovery after the 2008 Wenchuan earthquake. *Ecological Indicators*, *89*, 438-444.
- Yu, B., & Chen, F. (2017). A new technique for landslide mapping from a large-scale remote sensed image: A case study of Central Nepal. *Computers & Geosciences*, *100*, 115-124.
- Yunus, A.P., Fan, X., Tang, X., Jie, D., Xu, Q., & Huang, R. (2020). Decadal vegetation succession from MODIS reveals the spatio-temporal evolution of post-seismic landsliding after the 2008 Wenchuan earthquake. *Remote Sensing of Environment*, *236*, 111476.
- Zhao, C., Cao, X., Chen, X., & Cui, X. (2022). A consistent and corrected nighttime light dataset (CCNL 1992–2013) from DMSP-OLS data. *Scientific Data*, *9*, 424.

**Declaration of interests**

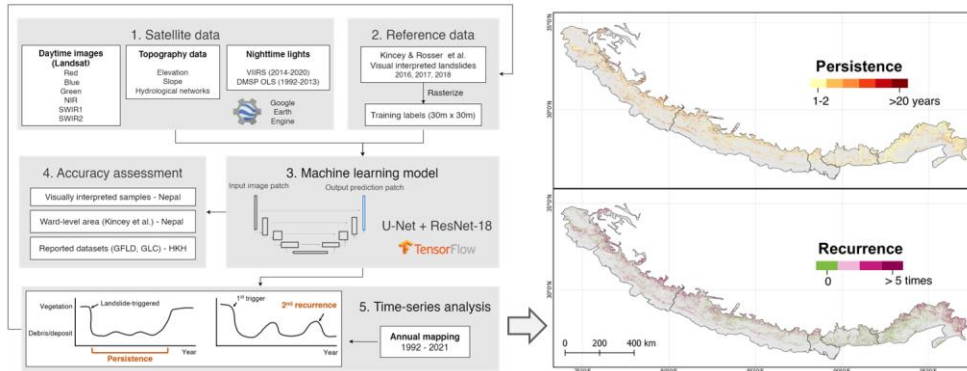
The authors declare that they have no known competing financial interests or personal relationships that could have appeared to influence the work reported in this paper.

The authors declare the following financial interests/personal relationships which may be considered as potential competing interests:

Karen C. Seto reports financial support was provided by NASA. Nick J. Rosser reports financial support was provided by UK Research and Innovation. If there are other authors, they declare that they have no known competing financial interests or personal relationships that could have appeared to influence the work reported in this paper.

Journal Pre-proof

## Graphical abstract



**Highlights:**

- Large-scale understanding of landslide dynamics is lacking for risk mitigation.
- We propose a method to detect recurrent and persistent landslides.
- 86% of landslide areas were persistent or recurrent in the Himalaya.
- 22% of landslide area experienced at least three episodes of landslides in 30 years.
- Transboundary landslide patterns related to anthropogenic, climate, and seismic factors.

Journal Pre-proof